Restitution methodology for space and time dependent solid-fuel port diameter evolution in hybrid rocket engines

Jean-Étienne Durand, Jean-Yves Lestrade, Jérôme Anthoine

Version of Record: https://www.sciencedirect.com/science/article/pii/S1270963821000092
Manuscript_4b68dea0e7ee2db40b69cd91f7fd9ee7

Restitution Methodology for Space and Time dependent Solid-Fuel Port Diameter Evolution in Hybrid Rocket Engines

Jean-Étienne Durand[a,1,*], Jean-Yves Lestrade[a,2], Jérôme Anthoine[a,3]

[a] *ONERA/DMPE, Université de Toulouse, F–31055 Toulouse, France*

Abstract

A post-processing tool for experimental data is developed to rebuild the instantaneous and local distributions of the fuel port diameter and the fuel regression rate throughout the port conduct during a firing test. The main objective is to use the developed methodology to be able, at a given instant during the firing test, to simulate a hybrid rocket engine configuration and to validate the related numerical modeling. The methodology is based on the coupling between the instantaneous fuel mass flow rate obtained by a ballistic reconstruction technique and the port diameter measurement throughout the port conduct after the firing test. The ballistic reconstruction method is adapted and applied to an experimental hybrid rocket, using hydrogen peroxide/high density polyethlylene propellants, with a catalytic injector (HYCAT). Firstly, a set of representative firing tests is selected from the HYCAT hybrid rocket engine testing campaign. Secondly, an analytical approach leads to instantaneous evolutions of the fuel port diameter and the fuel regression rate profiles throughout the fuel port conduct. The rebuilt profiles of the instantaneous port diameter show the ability of the methodology to restore the space and time distribution of the fuel port

*Fully documented templates are available in the elsarticle package on CTAN.
*Corresponding author
Email address: jean-etienne.durand@orange.fr (Jean-Étienne Durand)
[1]Ph.D. Candidate, Rocket Propulsion Laboratory Unit, Multi–Physics for Energetics Department; jean-etienne.durand@orange.fr.
[2]Research Scientist, Rocket Propulsion Laboratory Unit, Multi–Physics for Energetics Department; jean-yves.lestrade@onera.fr.
[3]Head of the Multi–Physics for Energetics Department; jerome.anthoine@onera.fr.

diameter. Nevertheless, the fuel regression rate distributions show some limitations of the methodology even though the average is coherent with the ballistic reconstruction trends.

Keywords: Hybrid Rocket Engine, Ballistic Reconstruction, Engine testing
2010 MSC: 00-01, 99-00

Nomenclature

Acronyms

HDPE	High density polethylene
US	Ultrasonic sensor

Complex quantities

ΔM	Mass loss between the final and initial states (g)
Δt	Time step (s)
Δt_{mes}	Pulse repetition period (s)
$\dot{m}$	Mass flow rate ($g.s^{-1}$)
η_c	Combustion efficiency
Λ	Fuel mass flow rate fraction in a port part
B	Relative peak intensity ratio (%)
$C^\star$	Characteristic velocity ($m.s^{-1}$)
M_{mp}	Fuel mass loss in a port part(g)
O/F	Oxidizer-to-fuel ratio

Function symbols

$\delta(X)$	Uncertainty of X
$\epsilon(X) = 100(X - X_{ref})/X_{ref}$	(%)
$\langle X \rangle_t$	Time-average of X
$\overline{X}$	Space-average of X

Geometric quantities

D	Diameter (mm)
L	Length (mm)
S	Section area (mm^2)
t	Time (s)
v_{lat}	Fuel regression rate on solid-fuel ends ($mm.s^{-1}$)
v_{reg}	Fuel regression rate ($mm.s^{-1}$)
z	Engine axis coordinate (mm)

Index symbols

$erod$	Throat erosion
exp	Experimental
ext	External lateral surface of the solid-fuel
fin	Final state
$fuel$	Fuel

	he	Solid-fuel head end		tof	Time-of-flight
	hyb	Hybrid phase		tot	Total
	ini	Initial state		**Physical quantities**	
	ox	Oxidizer		ρ	Density (g.s^{-1})
	$port$	Solid-fuel port		C_0	Sound speed (m.s^{-1})
	re	Solid-fuel rear end		f_s	Sample frequency (m.s^{-1})
	ref	Reference		M	Mass loss (g)
	th	Theoretical		P_{ch}	Chamber pressure (MPa)
	$throat$	Throat region		T	Temperature (K)

1. Introduction

The hybrid rocket engine (HRE) can offer a relevant alternative to solid and liquid propulsion systems in some space applications as apogee missions for geostationary satellites or suborbital transportation for tourism purposes. Safety is significantly enhanced because the propellants are split to avoid hazardous risks. Due to the diffusion-limited phenomenon observed by Marxman and Gilbert[1], thermochemical runaway does not occur contrary to solid propulsion. Furthermore, compared to liquid propulsion, HRE presents higher reliability as the plumb is greatly reduced. About throttle ability, the hybrid rocket engine can start, stop, restart, and modulate the thrust by controlling the oxidizer mass flow rate injected in the chamber. About performances, the specific impulse is higher than the values in solid rockets and comparable to the storable liquid engines. Beyond these technical advantages, the hybrid rocket is low-cost propulsion and presents a low impact on the environment.

Because experimental research, yet essential, is expensive and evolves according to the trials and error philosophy, numerical simulations can provide affordable and useful complementary data as the flow represented by the computational results can be easily accessed and handled. However, the validation of

the chosen numerical modeling needs to be assessed by comparing the computed and measured fuel regression rate behavior which plays a key role in controlling, through the fuel mass flow rate, the performances and efficiency of hybrid rocket.

In the literature, the comparison between testing and numerical simulation is mainly performed by the spatial and temporal averaged fuel regression rate values based on the port diameters measurements at the initial and the final states. The final port diameter is usually obtained by considering the mass loss during the firing test under the volume conservation assumption[2, 3, 4, 5, 6, 7, 8, 9, 10, 11, 12, 13]. Nevertheless the validation comparison process requires to be improved by considering the spatial variations of fuel regression rate along the port. Zhang *et al.*[14] have used this approach to study the impacts of diaphragms on the local fuel regression rate behavior. Also, Di Martino *et al.*[15, 16] have followed the same way to understand the thermal boundary layer effects on fuel regression rate for Hight Density Polyethylene (HDPE), Acrylonitrile Butadiene Styrene (ABS), and paraffin wax solid fuels. Kumar *et al.*[17] have improved the spatial validation for hybrid rocket configuration using an increasing linear profile for the port diameter along the axis of the engine instead of a constant port diameter. However, this approach cannot allow the fuel regression rate comparison to validate the instantaneous behavior provided by numerical modeling. Bianchi *et al.*[4] have used the instantaneous data from a ballistic reconstruction method developed by Carmicino and Russo Sorge[18] to validate with success the ability of a hybrid rocket configuration to represent the spatial and temporal average of the fuel regression rate. Nevertheless, the instantaneous fuel regression rate and the port diameter provided by the ballistic reconstruction method are assumed to be space-averaged throughout the fuel port. The ultrasonic sensors used in hybrid rocket testings (Bianchi *et al.*[4], Carmicino *et al.*[18], Lestrade *et al.*[19]) can provide local information of the instantaneous fuel regression rate. However, in all studies, too few sensors are used to get a fuel regression rate profile throughout the port. Furthermore, this technique requires very high accuracy to get reasonable uncertainty values,

compromised by the sound speed sensitivity to the solid-fuel thermo-physics.

Hence, in the current literature, the fuel regression rate behavior is analyzed only by splitting the temporal and spatial coordinates by averaging the quantities according to one of the two. Those approaches cannot comprehensively validate the numerical modeling used to simulate the intern ballistics of a hybrid rocket. Therefore, simultaneous spatial and temporal distribution is required.

At ONERA, numerical modeling of the intern ballistics of a hybrid rocket engine has been developed and requires to be validated. The fuel regression rate behavior computed numerically must represent the instantaneous fuel regression rate profile throughout the port during the firing test. A methodology is developed to rebuild the spatial and temporal distribution of the fuel regression rate and the port diameter based on the experimental data obtained from an HYCAT testing campaign with HDPE and catalytic H2O2 as propellants. Firstly, representative firing tests are selected from the testing campaign of the aforementioned hybrid rocket engine. The firing tests are classically analyzed. Secondly, the restitution methodology, based on the instantaneous fuel mass flow rate, and the direct measurement of the final port diameter is exposed. The instantaneous fuel mass flow rate is obtained by a ballistic reconstruction technique adapted for HYCAT firing tests. The analytical approach is presented and applied to the chosen firing test sample. The results are discussed and the scope for future improvements is drawn.

2. Experimental database from HYCAT testing campaign

The restitution methodology is based on the analysis of experimental data obtained from the HYCAT facility, an instrumented lab-scale engine (Figure 1).

2.1. Experimental set-up

The HYCAT facility is made up of four parts: a catalyzer injector, a combustion chamber, a post-chamber, and a nozzle. This facility was designed to

be able to change the length of each engine part and the fuel grain type [20]. Even though different propellants can be used, those involved in this paper are HDPE for the solid-fuel and spatial grade H_2O_2 for the oxidizer.

The engine, which can operate until 7.5 MPa, is instrumented with a Coriolis mass flowmeter for the oxidizer and four piezoelectric pressure probes (two just before the combustion chamber and two in the post-chamber) and is connected to a quartz three-component dynamometer thrust bench to get the propulsive performances. Temperature and pressure measurements of the liquid oxidizer just upstream of the injector are also included.

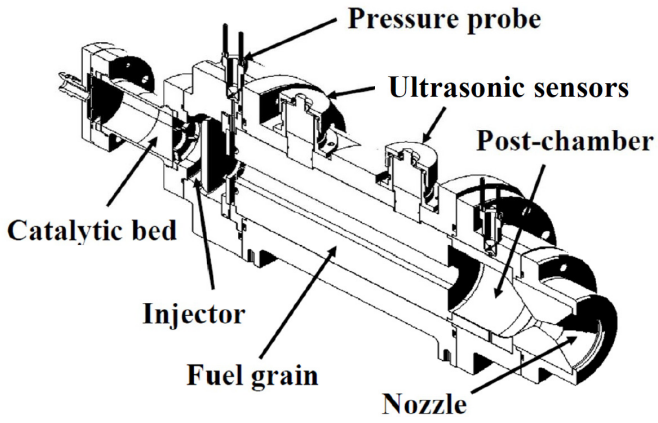

Figure 1: HYCAT facility.

To measure instantaneously the fuel regression rate, the engine is also instrumented with 1.0 MHz\1.0" ultrasonic sensors (one located at the head-end of the fuel grain and two at the rear-end)[21, 22]. Pulse-echo technique is nonintrusive and easy to set up compared with visualization and X-rays measurement techniques.

Table 1: Uncertainty and range of measurement instruments.

Instrument	Uncertainty	Range
Coriolis mass flow meter	0.1 %	0 - 2×10^{-1} kg.s^{-1}
3-Component dynamometer	0.2 %	0 - 2×10^{3} N
Piezoelectric pressure probe	0.2 %	7×10^{-3} - 1×10^{1} MPa

A catalytic injector, which enables the combustion efficiency to increase relative to a classical atomizer, is used[23]. The catalyzer decomposes the hydrogen peroxide into hot gaseous oxygen and steam water which is then injected through a gaseous injector directly within the combustion chamber without using a pre-chamber. The injection of a hot gaseous oxidizer is expected to improve the mixture with the pyrolysis gas provided by the fuel grain and to avoid losing a part of the generated heat flux to vaporize and warm the liquid oxidizer. The catalytic injector combines a liquid injector plate, a decomposition chamber containing the catalyst particles, and a gaseous injector (figure 2). The injector plate is designed to spread all the liquid hydrogen peroxide through the cross-section of the decomposition chamber. This chamber consists of an Inconel cylinder closed by refractory steel meshed to maintain the catalyst particles inside the decomposition chamber. The catalyst, developed and provided by Heraeus, is a Pt-based catalyst supported on Al_2O_3 material[24]. With the use of a catalytic bed, no pyrotechnic device is required to ignite the hybrid engine, improving safety. The ignition occurs owing to the energy supplied from the hot oxidizer flow. The catalytic bed has therefore to provide a very good efficiency related to a short transient time. A multi-pulsed operation of the hybrid engine is thereby possible as well.

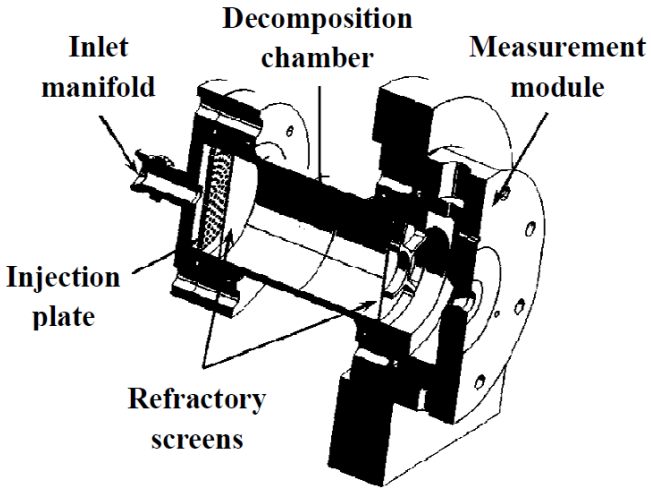

Figure 2: Catalytic injector.

The decomposition temperature is measured at the outlet of the catalytic bed thanks to three type K thermocouples with an uncertainty estimated at ± 1 K. The measurement of the decomposition chamber pressure enables to obtain the characteristic curve (oxidizer mass flow rate as a function of the pressure differential) of this chamber to precisely control the operating conditions of the mono-propellant tests and the hybrid firing tests. The synoptic diagram of the measurement chain is indicated in figure 3.

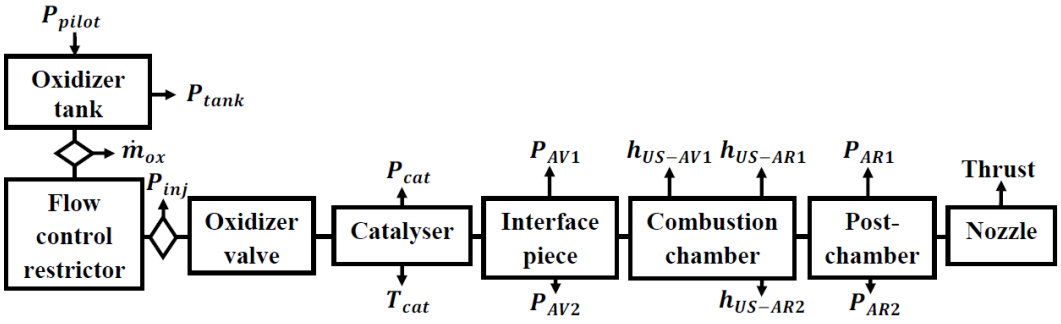

Figure 3: Synoptic diagram of the measurement chain of the HYCAT hybrid engine.

According to Lestrade *et al.*[23], the repeatability of the firing tests has been evidenced by comparing two tests performed in the same conditions. The reproducibility error is under 0.6 % for the mean pressure chamber, the characteristic velocity, and the mean thrust, except for the oxidizer-to-fuel ratio with a difference of 1.8 %.

2.2. Testing database

Four firing tests are selected from 26 HYCAT firing tests, performed with HDPE solid-fuel and 87.5w%-H_2O_2 oxidant, according to its representativeness of the database (table 2). Two kinds of injection configurations are tested: axial and swirl injection configurations. In the choked regime, the pressure level is obtained by using nozzles, using two values of throat diameter: 7 and 12.4 mm. From the first to the 24th firing test, the oxidizer mass flow rate is valued at around 100 g.s^{-1}. The 25^{th} and the 26^{th} HYCAT tests are performed with an oxidizer mass flow rate equal to 175 g.s^{-1} and 202 g.s^{-1}, respectively, in axial configuration, with a throat diameter set at 12.4 mm.

- The 12^{th} HYCAT firing test is the chosen reference firing test with axial injection;
- The 18^{th} HYCAT firing test is selected to represent the swirl injection case;
- The 23^{rd} HYCAT firing test is taken to display the pressure range with the HYCAT 12 firing test, by altering the nozzle throat section diameter.
- The 26^{th} HYCAT firing test is fulfilled to represent the range of oxidizer mass flow rate with the HYCAT 23 firing test.

All the firing tests are performed with an initial solid-fuel length equal to 240 mm and a constant fuel port diameter equal to 25 mm. The 25^{th} firing test, even though not treated here, is realized with similar conditions as the HYCAT 26 firing test with an oxidizer mass flow rate equal to 175 g.s^{-1}. Because the hybrid phase does not shorten enough and the high oxidizer mass flow rate level, the

carbon throat turns out to undergo erosion with a final throat diameter equal to 13.05 mm. According to the figure 4, the chamber pressure increases very slightly until t =10.76 s before slightly decreasing until the end of the firing test. Nevertheless, these variations are small compared with the mean chamber pressure value.

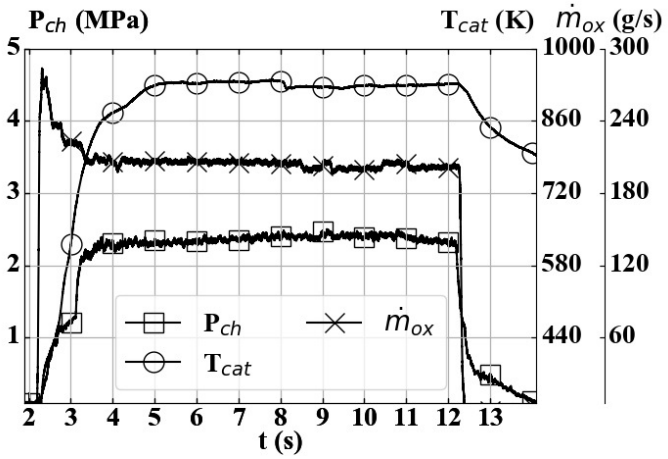

Figure 4: Pressure evolution for HYCAT 26 firing test.

Table 2: Configuration data for chosen firing tests.

Case	HYCAT 12	HYCAT 18	HYCAT 23	HYCAT 26
Targeted oxidizer mass flow rate ($g.s^{-1}$)	100	100	100	200
D_{throat} (mm) ($\pm$ 0.05 mm)	7.0	7.0	12.4	12.4
Injection configuration	axial	swirl	axial	axial

Figure 5 provides the temporal evolutions of the combustion chamber pressure, the oxidizer mass flow rate and the oxidizer decomposition temperature, and the thrust for the hybrid test for the HYCAT 12 case which is representative of a typical firing test in the HYCAT testing campaign.

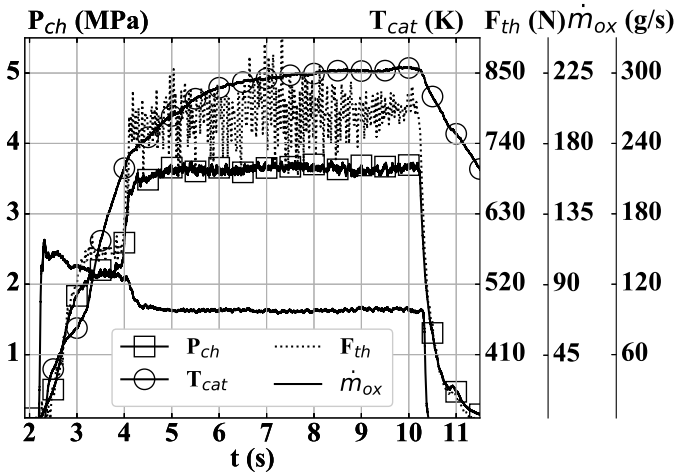

Figure 5: HYCAT 12 firing test.

A mono-propellant phase precedes the hybrid phase. When the combustion occurs, the diffusion flame increases the chamber temperature and then the characteristic velocity with the effect to provide a higher combustion chamber pressure. This pressure increase reduces the oxidizer mass flow rate compared to its amplitude during the mono-propellant phase. Larger pressure oscillations occurred for the axial injector case compared with the swirl injector case in which mixing is enhanced between the hot gaseous oxidizer and the pyrolyzed fuel [20]. The time variations of the thrust are very noisy compared with the other physical quantities.The pressure perturbations close to the throat are amplified through the divergent nozzle causing significant thrust variations.In fact, along the nozzle axis, the thrust increases when the flow exhausts in the divergent nozzle. Close to the nozzle, the pressure perturbations, associated with velocity perturbations as well, are transmitted to the thrust. Thus, when the thrust increases, the associated disruptions are amplified, becoming significant at the nozzle exit. The temperature recorded at the outlet of the decomposition temperature reaches about 875 K, just before the extinction of the engine.

For each firing test, the burning time, the global oxidizer-to-fuel ratio, the

mean oxidizer mass flow rate, the mean chamber pressure, and the mean oxidizer temperature during the hybrid phase are computed from the taken instantaneous data and the mass difference between the moments before and after the firing test. The burning time is obtained by measuring the difference of instants materialized by two peaks of the quadratic module of the time derivative of chamber pressure. Those peaks correspond to the sharp increase in pressure at the combustion process ignition and the sharp decrease at the quenching (Figure 6).

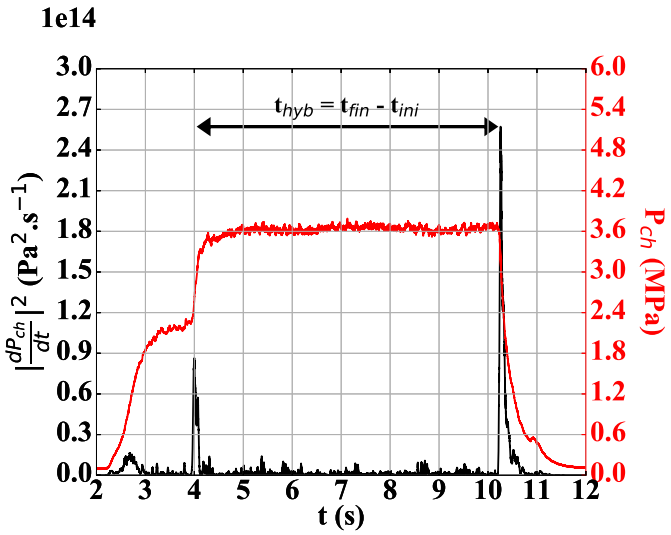

Figure 6: Method for determining the burning time.

The burning time uncertainty is nevertheless difficult to estimate because the final instant wherein the fuel consumption is altogether ended cannot be determined. Carmicino *et al.*[25] have proposed a methodology to estimate the burning time uncertainty by considering the time differences defined between two pressure regime levels for the initial and final instants. However, applying this approach to the HYCAT firing test data, the uncertainty is therefore estimated at 2.2 s for the HYCAT 12 case, corresponding to 35 % of the burning time value equal to 6.3 s. Just after the oxidizer valve closing, the chamber pressure decrease is less and less sharp with the time (combustion chamber

draining) leading to a final state difference equal to 4 s. Even though the aforementioned method takes into account comprehensively the time range related to the fuel mass loss during the firing test, the uncertainty is overestimated. In the present study, another approach is used and based on the temporal difference between the peak of a quadratic module time derivative of the chamber pressure (corresponding to the initial and final states) and, located on lobe base, the curve point of relative intensity B equal to 1 % of the reference peak (figure 7). Practically, to obtain clear peaks and related lobes, the chamber pressure time derivative is filtered by the Savitzky-Golay approach[26], before operating the squaring.

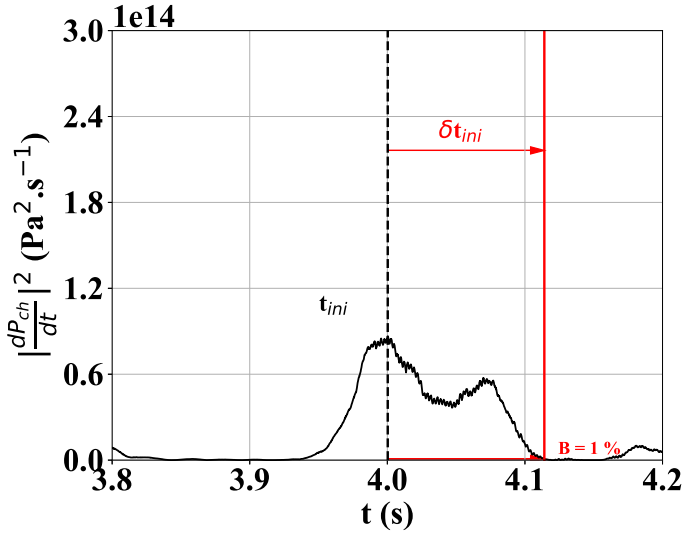

Figure 7: Initial instant uncertainty estimation method.

The uncertainty is computed according to the uncertainty propagation method:

$$\delta\left(t_{hyb}\right) = \sqrt{\delta t_{ini}^2 + \delta t_{fin}^2} \tag{1}$$

The burning time uncertainty of the HYCAT 12 case is therefore estimated to 0.4 s, corresponding to 6.6 % of the burning time value.

The time averaged fuel mass flow rate $\langle \dot{m}_{fuel} \rangle_t$ is obtained by measuring the mass loss during the firing test over the burning time:

$$\langle \dot{m}_{fuel} \rangle_t = \frac{\Delta M_{fuel}}{t_{hyb}} \tag{2}$$

Even though ΔM_{fuel} takes into account all mass losses during the firing test, the actual mass loss during the hybrid phase is necessarily lower due to the burnt fuel mass during the mono-propellant phase and just after the oxidizer valve closing. Nonetheless, those losses can be taken into account by the uncertainties related to the instants defining the initial and the final steps. Those instants correspond to the inflection points of chamber pressure evolution, which indicate indirectly the ignition and the quenching of the combustion process. The related steps describe the brief and sharp alteration of the chamber pressure level in which the combustion process ignites or, inversely, the fuel pyrolysis lessens until to be neglected.

Thereby the uncertainty method used in the present study takes into account the mass losses during the ignition and the quenching of the combustion process. With the same approach, the time-averaged oxidizer-to-fuel ratio is therefore expressed by:

$$\langle O/F \rangle_t = \frac{\langle \dot{m}_{ox} \rangle_t t_{hyb}}{\Delta M_{fuel}} \tag{3}$$

The combustion efficiency is computed according to the ratio of experimental to theoretical characteristic velocities $C^\star$:

$$\eta_c = \frac{C^\star_{exp}}{C^\star_{th}} \quad \text{where} \quad C^\star_{exp} = \frac{\langle P_{ch} \rangle_t S_{throat}}{\langle \dot{m}_{ox} \rangle_t + \langle \dot{m}_{fuel} \rangle_t} \quad \text{with} \quad S_{throat} = \frac{\pi D^2_{throat}}{4} \tag{4}$$

The theoretical characteristic velocity $C^\star_{th}$ is computed from the thermochemical equilibrium software NASA CEA[27]. The results of the selected firing tests are displayed in the table 3.

Table 3: Firing test results.

Case	HYCAT 12	HYCAT 18	HYCAT 23	HYCAT 26
t_{hyb} (s)	6.3 ± 0.4	3.2 ± 0.5	17.3 ± 0.7	9.1 ± 0.4
$\langle \dot{m}_{ox} \rangle_t$ (g.s^{-1})	97.7 ± 0.2	99.2 ± 0.2	105.0 ± 0.2	204.3 ± 0.5
$\langle P_{ch} \rangle_t$ (MPa)	3.6 ± 5.0 × 10^{-3}	4.4 ± 5.0 × 10^{-3}	1.2 ± 5.0 × 10^{-3}	2.4 ± 5.0 × 10^{-3}
ΔM_{fuel} (g)	50.0 ± 0.2	51.0 ± 0.2	135.0 ± 0.2	140.1 ± 0.2
$\langle O/F \rangle_t$	12.4 ± 0.8	6.3 ± 0.9	13.5 ± 0.6	13.7 ± 0.6
η_c	0.88 ± 0.02	0.91 ± 0.02	0.89 ± 0.01	0.89 ± 0.01

3. Methodology to restitute the time-space behavior of fuel regression rate

During the firing test, the ultrasonic sensors can provide local and instantaneous measurements. However, in the HYCAT configuration, two sensors are used to get a geometrical variation throughout the solid fuel. Consequently, only a mean value of fuel regression rate between the local measurements can be obtained. A series of small ultrasonic sensors is therefore needed to be able to rebuild a discretized fuel regression profile throughout the solid fuel instantaneously. Besides, from instantaneous measured global data, a method based on the evolution of characteristic velocity with a constant combustion efficiency can also provide an instantaneously space-averaged value of fuel regression rate. Only space-averaged data can be therefore treated instantaneously. In this testing campaign, the final variations of the fuel port diameter throughout the solid-fuel are the unique geometric data obtained after the firing test.

Hence, the instantaneous and geometric data are uncoupled. To get the time and space distribution of the fuel port diameter and the fuel regression rate, a restitution methodology is developed by linking these two kinds of data.

In the present study, the methodology is based on the final fuel port diameter

measurements after the firing test and the instantaneous fuel mass flow rate (figure 8).

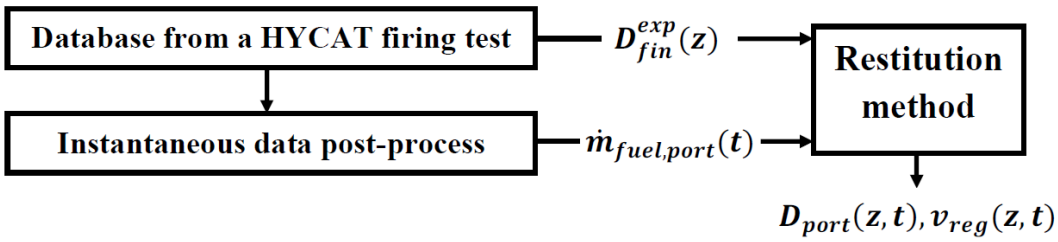

Figure 8: Methodology for time and spatial fuel regression rate distribution.

Firstly, the theory of restitution method is explained and developed. The experimental data are then post-processed to obtain both required inputs: the final fuel port diameter variations throughout the solid-fuel and the instantaneous fuel mass flow rate.

3.1. The restitution method: theoretical development

3.1.1. Implementation of the mass conservation equation in the fuel port conduct

The restitution methodology uses an analytical approach to rebuild the spatial and temporal fuel regression rate behavior.

The origin of the axis is located at the head end position of the solid fuel at the initial instant. z is the longitudinal coordinate throughout the engine axis $\vec{z}$ in the solid fuel port conduct. t is the time coordinate during the hybrid phase. The initial instant is related to the beginning of the hybrid phase. The fuel degradation is assumed axis-symmetric during the firing test. The elementary solid-fuel port log included between z and $z + dz$ is therefore assumed cylindrical. The fuel port diameter and fuel regression rate variations are invariant in rotation according to the axis $\vec{z}$ (figure 9).

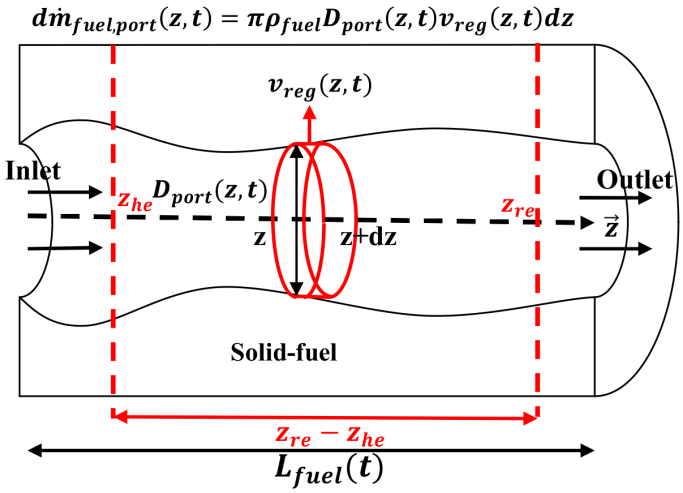

Figure 9: Elementary view of fuel mass flow rate in the fuel port and Application field of the restitution method.

Consequently, at t instant and z position, the elementary fuel mass flow rate through the port log with dz thickness is expressed by:

$$d\dot{m}_{fuel,port}\,(z,t) = \pi\rho_{fuel}D_{port}\,(z,t)\,v_{reg}\,(z,t)\,dz \tag{5}$$

Theoretically, the integration length of the elementary fuel mass flow rate in the fuel port should correspond to the instantaneous fuel port length at the instant t. However, because of several aero-thermo-chemical phenomena at the ends of solid-fuel port conduct such as the solid fuel melting, the liquid fuel phase movement, or likely heterogeneous surface reactions, the assumption of fuel regression is hardly justified or even senseless.

As stated in section 3.2, the observed bulge of melted HDPE at the fuel port inlet shows a lower value of fuel port diameter than measured initially and cannot be only altered by pyrolysis degradation.

The presented methodology is based on the fuel port diameter measurements throughout the fuel port conduct after the firing test. The sum of elementary

fuel mass flow rate operates therefore along the axis coordinate in a fixed measurement range of the final fuel port diameter. The minimal and maximal axis coordinates of this range are respectively z_{he} and z_{re}. Considering such an approach, the integration length does not depend on time. However, the knowledge of the *the fuel mass flow rate fraction* related to a given part of the fuel port conduct ($\Lambda(t)$) is required. The fuel mass flow rate produced in that part ($Q(t)$) defined by the positions z_{he} and z_{re} is thereby expressed by the formula:

$$\begin{cases} \forall t \in [t_{ini}, t_{fin}], \quad \Lambda(t) = \dfrac{Q(t)}{\dot{m}_{fuel,port}(t)} \\ Q(t) = \pi \rho_{fuel} \displaystyle\int_{z_{he}}^{z_{re}} D_{port}(z,t)\, v_{reg}(z,t)\, dz \end{cases} \tag{6}$$

Besides, a partial differential equation can be built organically from the fuel regression rate definition:

$$\forall t \in [t_{ini}, t_{fin}], \quad \frac{\partial D_{port}}{\partial t}(z,t) = 2 v_{reg}(z,t) \tag{7}$$

The mass conservation equation (6) can therefore be written as:

$$\forall t \in [t_{ini}, t_{fin}], \quad \frac{2Q(t)}{\pi \rho_{fuel}} = \int_{z_{he}}^{z_{re}} D_{port}(z,t) \frac{\partial D_{port}}{\partial t}(z,t)\, dz \tag{8}$$

According to the Leibniz integral rule, a time dependent differential equation can be established:

$$\forall t \in [t_{ini}, t_{fin}], \quad \frac{4Q(t)}{\pi \rho_{fuel}} = \frac{d}{dt}\left(\int_{z_{he}}^{z_{re}} D_{port}(z,t)^2\, dz \right) \tag{9}$$

Assuming the knowledge of the fuel mass flow rate fraction $\Lambda(t)$ and the total fuel mass flow rate in port, the fuel mass flow rate $Q(t)$ over the measured port part is altogether known. Thus, the instantaneous fuel mass loss $M_{mp}(t)$ in the measured port part is known as well. The antiderivative of the equation 9 is expressed as:

$$\forall t \in [t_{ini}, t_{fin}], \quad \frac{4M_{mp}(t)}{\pi \rho_{fuel}} + K = \int_{z_{he}}^{z_{re}} D_{port}(z,t)^2\, dz \quad \text{and} \quad M_{mp}(t) = \int_{t_{ini}}^{t} Q(u)\, du \tag{10}$$

where K is a real constant. However, at the beginning of the hybrid phase, the solid fuel is assumed without mass loss and the initial port diameter is constant

throughout the port conduct. The constant K is therefore valued as:

$$K = (z_{re} - z_{he})\, D_{ini}^2 \tag{11}$$

whence the equation ruling the mass conservation related to the local port diameter throughout the solid fuel:

$$\forall t \in [t_{ini}, t_{fin}]\,, \quad \frac{4M_{mp}(t)}{\pi \rho_{fuel}} + (z_{re} - z_{he})\, D_{ini}^2 = \int_{z_{he}}^{z_{re}} D_{port}(z,t)^2\, dz \tag{12}$$

The previous equation governs the time evolution of the fuel port diameter during the hybrid phase in order to respect the conservation of the fuel mass flow rate instantaneously in the port. However, the port diameter depends not only on the time but also on the axial coordinate z throughout the solid-fuel. In the presented approach, the measurement of the port diameter variations throughout the solid-fuel at the final instant or after the firing test defines a boundary condition of the system. Furthermore, at the initial instant, the port diameter is assumed constant throughout the solid fuel:

$$\forall z \in [z_{he}, z_{re}]\,, \quad D_{port}(z, t_{ini}) = D_{ini} \quad \text{and} \quad D_{port}(z, t_{fin}) = D_{fin}^{exp}(z) \tag{13}$$

3.1.2. Determination of the coupling equation

To close the system, an equation describing the fuel port diameter variations throughout the solid-fuel for each instant t, is required and must be provided by the heat flux distribution at the fuel surface. This field is the results of aerothermochemical phenomena occurring in the port. However, the related parameters are not directly available from data obtained during the firing test. Nevertheless, to build the presented methodology, the trends and the positions of the spatial variations of the turbulent boundary layer and the non-premixed flame during the firing test are assumed conserved throughout the fuel port conduct whatever their time evolution. Those variations are therefore printed instantaneously by the convective heat flux on the fuel regression rate distribution throughout the fuel port conduct. At the final state, the observed port diameter variations thereby correspond to the spatial footprint left by the combustion process in the port during the firing test. Hence, as the instantaneous

spatial port diameter variations reflect the ones measured after the firing test, the required additional equation states that *for each instant of the hybrid phase, the spatial port diameter variation is proportional to the one at the final state*:

$$\forall (z,t) \in [z_{he}, z_{re}] \times [t_{ini}, t_{fin}], \quad \frac{\partial D_{port}}{\partial z}(z,t) = \frac{dD_{fin}^{exp}}{dz}(z)\,\theta(t) \tag{14}$$

The θ coefficient is not assumed constant and shapes a time dependent C^1 class function defined as:

$$\theta : \left| \begin{array}{ccc} [t_{ini}, t_{fin}] & \longrightarrow & [0,1] \\ t & \longmapsto & \theta(t) \end{array} \right. \quad \text{with} \quad \theta(t_{ini}) = 0 \quad \text{and} \quad \theta(t_{fin}) = 1$$

Because the port diameter is constant throughout the solid-fuel port conduct at the beginning of the initial state, the function θ must be equal to zero. Besides, the port diameter variations at the final state must correspond to the one measured experimentally after the firing test. The value of the function θ is therefore equal to 1.

3.1.3. Equation resolution

] Thus, a solution can be found for the established system assuming the decoupling between the two variables z and t and is expressed as:

$$\forall (z,t) \in [z_{he}, z_{re}] \times [t_{ini}, t_{fin}], \quad D_{port}(z,t) = \left(D_{fin}^{exp}(z) - D_{ini}\right)\theta(t) + D_{ini} \tag{15}$$

In order to determine the time evolution of θ function, the considered solution is injected in the equation (12). After reduction, a 2^{nd} order polynomial equation is found:

$$\forall t \in [t_{ini}, t_{fin}], \quad \sigma^{+}\theta(t)^2 + 2D_{ini}\sigma_0\theta(t) - \frac{4M_{mp}(t)}{\pi\rho_{fuel}} = 0 \tag{16}$$

where:

$$\sigma^{+} = \int_{z_{he}}^{z_{re}} \left(D_{fin}^{exp}(z) - D_{ini}\right)^2 dz \quad \text{and} \quad \sigma_0 = \int_{z_{he}}^{z_{re}} \left(D_{fin}^{exp}(z) - D_{ini}\right) dz \tag{17}$$

The related discriminant is strictly positive, implying two real solutions for the equation (16), for each instant of the hybrid phase:

$$\forall t \in [t_{ini}, t_{fin}], \quad \Delta(t) = 4D_{ini}^2\sigma_0^2\left(1 + \frac{4\sigma^{+}M_{mp}(t)}{\pi\rho_{fuel}D_{ini}^2\sigma_0^2}\right) > 0 \tag{18}$$

Only one of the two is positive. Analytically, the θ function is therefore written as:

$$\forall t \in [t_{ini}, t_{fin}], \quad \theta(t) = \frac{D_{ini}\sigma_0}{\sigma^+}\left(\sqrt{1 + \frac{4\sigma^+ M_{mp}(t)}{\pi\rho_{fuel}D_{ini}^2\sigma_0^2}} - 1\right) \tag{19}$$

Analytical expressions of the time-space distribution for the fuel regression rate and port diameter are thereby:

$$\forall (z,t) \in [z_{he}, z_{re}]\times[t_{ini}, t_{fin}], \quad v_{reg}(z,t) = \left(\frac{D_{fin}^{exp}(z)}{D_{ini}} - 1\right)\frac{Q(t)}{\pi\rho_{fuel}\sigma_0\sqrt{1 + \frac{4\sigma^+ M_{mp}(t)}{\pi\rho_{fuel}D_{ini}^2\sigma_0^2}}} \tag{20}$$

$$\text{and} \quad D_{port}(z,t) = \frac{\left(D_{fin}^{exp}(z) - D_{ini}\right)D_{ini}\sigma_0}{\sigma^+}\left(\sqrt{1 + \frac{4\sigma^+ M_{mp}(t)}{\pi\rho_{fuel}D_{ini}^2\sigma_0^2}} - 1\right) + D_{ini}$$

3.1.4. Determination of $\Lambda(t)$

The final fuel port diameter profile and the fuel mass flow rate in the considered port part need to be known to use the aforementioned distributions. Hence, the evolution of $\Lambda(t)$ must be determined throughout the hybrid phase. This quantity cannot unfortunately be characterized from the established equations. Nevertheless, theoretically, the fuel mass flow rate produced in the whole port can be used, i.e. $\Lambda(t) = 1$, if the considered port part in the diameter measurement covers entirely the solid-fuel port instantaneously.

For HYCAT firing tests, the bulges observed at the fuel port ends do not allow to take into account systematically the whole port. Consequently, the fuel mass flow rate fraction is strictly lower than 1. Nevertheless, the fuel port part taken by the bulges is small (9 - 13 mm) relatively to the fuel length (240 mm). Considering a solid-fuel port part without the bulge regions, the variations of $\Lambda(t)$ are therefore limited. Consequently, the temporal evolution of $\Lambda(t)$ can be, at the 1^{st} order, neglected. The fuel mass flow rate fraction is thereby assumed constant Λ_0. The fuel mass flow rate of the considered port part is therefore proportional to the one produced in the port.

$$\forall t \in [t_{ini}, t_{fin}], \quad Q(t) = \Lambda_0 \dot{m}_{fuel,port}(t) \tag{21}$$

The fuel mass flow rate fraction value can be determined by integration of the equation 21. Λ_0 becomes the mass loss ratio between the considered port log and the whole port.

$$\forall t \in [t_{ini}, t_{fin}], \quad M_{mp}(t) = \Lambda_0 M_{fuel,port}(t) \quad \text{with} \quad M_{fuel,port}(t) = \int_{t_{ini}}^{t} \dot{m}_{fuel,port}(u)\, du \tag{22}$$

At the end of the firing test, the fuel mass loss during the firing test on the considered part M_{mp}^{fin} is limited by the condition imposed by the equation (16) with $\theta(t_{fin}) = 1$:

$$M_{mp}^{fin} = \frac{\rho_{fuel}\pi}{4}\left(\sigma^{+} + 2D_{ini}\sigma_0\right) \tag{23}$$

Computing geometrically the mass loss on the considered part with the 2^{nd} wording of the Guldin's theorem, the expression of the equation (23) is also found:

$$M_{mp}^{fin} = \rho_{fuel}(2\pi r_G \sigma_0) \quad \text{with} \quad r_G = \frac{1}{\sigma_0}\int_{z_{he}}^{z_{re}} \int_{\frac{D_{ini}}{2}(z)}^{\frac{D_{fin}^{exp}}{2}(z)} r\, dr dz \tag{24}$$

Hence, the limiting mass at the final instant of the firing test determining the validity of the modeling corresponds exactly to the mass lost physically in the considered part, showing the coherence of the presented approach. The fuel mass flow rate fraction related to the measured solid fuel part is therefore obtained by the following expression:

$$\Lambda_0 = \frac{\rho_{fuel}\pi}{4M_{fuel,port}^{fin}}\left(\sigma^{+} + 2D_{ini}\sigma_0\right) \tag{25}$$

The restitution methodology needs two input data to rebuild the time and space distribution of fuel port diameter and regression rate:

- Input 1: the final fuel port diameter profile throughout the solid fuel is measured after the firing test
- Input 2: the ballistic reconstruction method is used to determine the instantaneous fuel mass flow rate during a firing test.

3.2. *Input 1: fuel port diameter measurement throughout the solid-fuel*

The final fuel port section diameter varies with the solid-fuel length. To measure these variations into the port conduct, the solid-fuel is cut regularly in eight slices with, each of them, a thickness of 30 mm (figure 10).

Figure 10: Slices of the solid-fuel after the firing test.

The fuel port section is assumed circular. The port diameter measurement uncertainty takes thereby into account the observed deformation due to the asymmetry of the combustion process in the port during the firing test. Consequently, the local final fuel port diameter measurement is obtained with an interior micrometer for each position defined by the slicing.

The final port diameter profile throughout the solid-fuel port conduct for the HYCAT 12 case is shown in figure 12. Surprisingly, the final fuel port diameter located at z = 9 mm, equal to 23.3 mm, is lower than the initial fuel port diameter, corresponding to the observed bulge of melted HDPE at the port inlet region (figure 11). This phenomenon could occur when the HDPE is insufficiently heated at the head end face of the solid-fuel, leading to a thaw instead of pyrolysis.

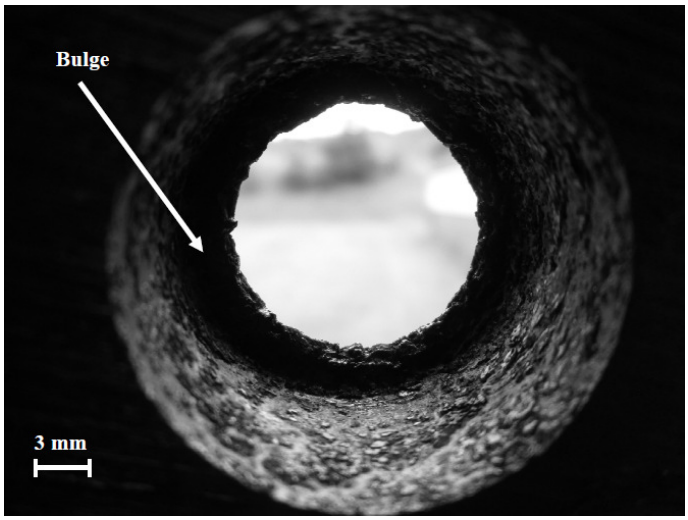

Figure 11: Bulge formed at the port inlet.

The melted HDPE would be dragged towards the port inlet until the pyrolysis process starts. Permanently fed in melted HDPE, the port inlet region holds a section diameter slightly lower than the initial diameter.

Downstream the bulge, the port diameter profile draws a parabolic convex curve with a minimum value equal to 28.8 mm, at z = 120 mm. Classically, the decrease in fuel regression throughout the first part of solid-fuel conduct is due to less stiff boundary layer temperature and velocity gradients at the fuel surface as the turbulent boundary layer increases in the downstream direction[28]. However, from z= 120 mm, the fuel regression rate starts increasing because of the total mass flux increase throughout the solid-fuel as fuel degradation is mainly due to the thermal convection. Hence, the studied case is coherent with the previous explanation. The final port diameter profiles related to the 18^{th}, 23^{rd} and 26^{th} firing tests also display a local minimum value at z = 120 mm. However, in the region between z = 30 mm and z = 120 mm, the fuel port diameter profiles show that the fuel regression rate level is greater close to the port inlet than in the port outlet.

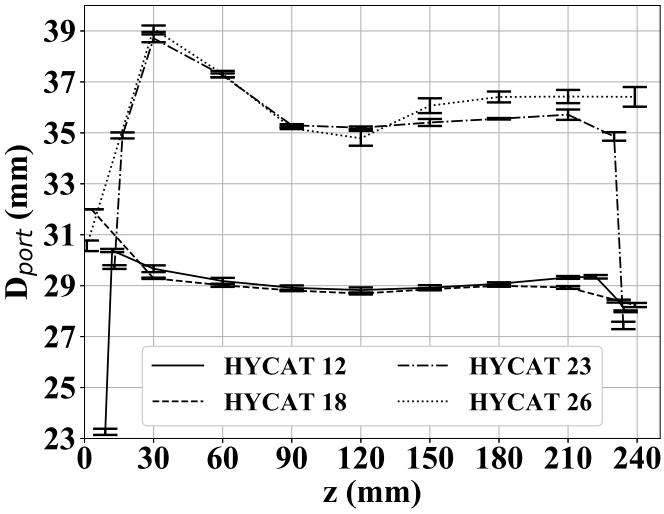

Figure 12: Final port diameter profile throughout the solid fuel for the considered HYCAT firing tests.

No bulge appears for the HYCAT 18 and 26 cases. Instead, the fuel surface in the inlet region shapes a truncated cone because of the coupling effect between the injection ring and the oxidizer injection condition. In fact, for the HYCAT 18 case, the oxidizer inflow swirls through the ring. For the HYCAT 26 case, the oxidizer mass flow rate, injected axially, is twice higher than the value assessed in the other firing tests. The flow inertia is, therefore, an essential phenomenon to take into account for the bulge formation.

Between z = 120 mm and z = 210 mm, the HYCAT 12 and 23 cases show a gradual increase in the fuel port diameter before decreasing dramatically. For the HYCAT 18 firing test, the decrease is much slighter. The HYCAT 26 case, however, displays, downstream z = 180 mm, an almost constant variation of the port diameter until the outlet. This particular region shows a wave-patterned fuel surface. This kind of pattern would result from the development of small vortices strengthened throughout the conduct as suggested by Koo *et al.*[29]. The heat transfer is thereby oscillating, causing the observed uneven fuel surface.

The same phenomenon is reproduced for the non-treated case HYCAT 25 using an oxidizer mass flow rate equal to 175 g.s^{-1}. Figure 13 shows the longitudinal cut of the solid fuel.

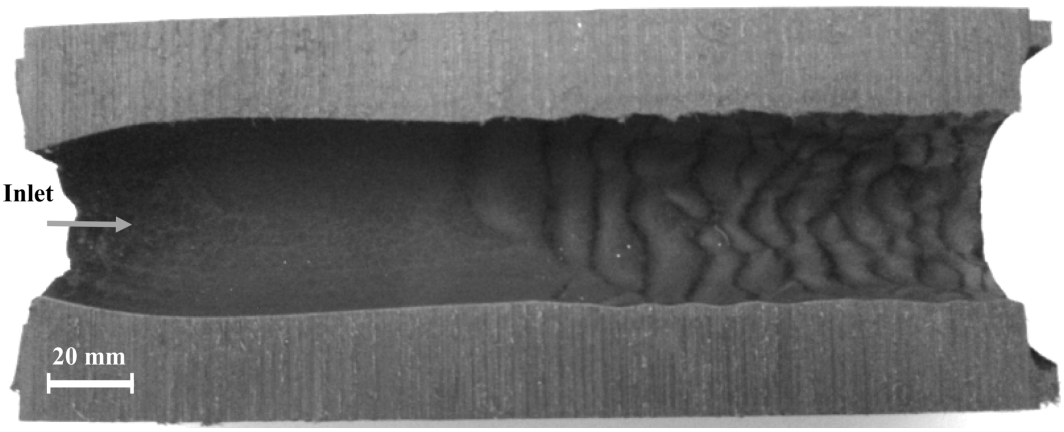

Figure 13: HYCAT 25: longitudinal cut of the solid fuel after the firing test.

However, the fuel surface pattern obtained by Koo *et al.* is found throughout the solid-fuel port conduct contrary to the observation in HYCAT 25 and 26 firing test cases. Further studies are required to clearly understand the transition between the classical theory of fuel degradation and the phenomena carving the solid-fuel to form a wave-patterned surface. Hence, the use of a high oxidizer mass flow rate value, around 200 g.s-1, may lead to trigger a new fuel degradation mode. Consequently, the use of an oxidizer mass flow rate around 200 g.s^{-1} may lead to trigger a new fuel degradation mode involving liquefaction property of HDPE.

The spatially averaged final port diameter can be computed by considering an integral method:

$$\overline{D}_{fin}^{exp} = \frac{1}{z_{re} - z_{he}} \int_{z_{he}}^{z_{re}} D_{fin}^{exp}(z)\, dz \tag{26}$$

The degradation of the head and rear end surfaces of the solid-fuel cannot be

neglected because of the low fuel regression level of the HDPE. In fact, for the HYCAT 12 firing test, the total ablated fuel length is 2 mm, large enough to represent 14.4 % of the total mass loss during the firing test. The use of the direct measurements of the port diameter to determine the fuel regression rate is therefore suitable. The spatial and temporal average of the fuel regression rate in the solid-fuel port conduct is obtained by the formula:

$$\langle \overline{v}_{reg} \rangle_t = \frac{\overline{D}_{fin}^{exp} - D_{ini}}{2t_{hyb}} \tag{27}$$

The fuel regression velocity on the solid-fuel ends assumes to take into account the regression for both ends together. Hence, an estimation is obtained by measuring the fuel length differences between the initial and the final states:

$$v_{lat} = \frac{L_{fuel,ini} - L_{fuel,fin}}{t_{hyb}} \tag{28}$$

Because the head and rear end surfaces are not plane at the end of the firing test, several types of the sliding caliper and depth gauges are used to measure the equivalent fuel length. With this fuel regression rate value at the ends of the solid-fuel, the fuel mass flow rate can therefore be estimated (table 4).

Considering the HYCAT firing tests, the final diameters obtained by direct measurements, the time and space averaged fuel regression rate in the port and on the solid-fuel ends are given in the table 4.

Table 4: Space averaged final port diameter and space and time averaged fuel regression rate for the selected firing tests.

Case	HYCAT 12	HYCAT 18	HYCAT 23	HYCAT 26
$\overline{D}_{fin}^{exp}$ (mm)	29.1 ± 0.3	29.1 ± 0.1	35.8 ± 0.4	36.1 ± 0.7
$\langle \overline{v}_{reg} \rangle_t$ ($\mathrm{mm.s^{-1}}$)	0.34 ± 0.03	0.64 ± 0.10	0.32 ± 0.02	0.61 ± 0.05
$L_{fuel,ini} - L_{fuel,fin}$ (mm)	2.0	2.4	5.4	2.3
v_{lat} ($\mathrm{mm.s^{-1}}$)	0.3	0.7	0.3	0.3

3.3. Input 2: instantaneous fuel mass flow rate in the solid-fuel port conduct.

Several techniques are available to measure the instantaneous fuel regression rate, such as the ultrasonic pulse-echo, resistance-based, x-ray radiography, microwave, and plasma capacitance gauge methods. In the present study, to catch temporal variations of fuel regression rate during a firing test, the ultrasound measurement has been used during the testing campaign. As the sound speed is sensitive to temperature, the fuel regression rate obtained from ultrasound measurement is influenced by the temperature distribution in the fuel. Nevertheless, according to Sorge and Carmicino[30], as the HDPE has a low thermal diffusion value (0.23 $mm^2.s^{-1}$), the error in fuel regression rate, is lower than 1.5 %. Unfortunately, the testing campaign data cannot be successfully treated because of anomalous trends of the time-to-flight variations with the time. In fact, during the mono-propellant phase, the solid-fuel is heated, introducing a non-negligible temperature profile before the beginning of the hybrid phase. A methodology to correct such phenomenon is currently under development at ONERA to conveniently seize the fuel port diameter evolution.

Hence, in the present study, the instantaneous spatially averaged fuel regression rate is obtained by using the ballistic reconstruction method based on instantaneous data of chamber pressure, catalytic temperature, and oxidizer mass flow rate during a firing test. With such an approach, the instantaneous fuel mass flow rate in the port can be determined easily and used for the restitution technique.

Wernimont and Heister[31] have built an integral technique to determine the instantaneous fuel regression rate by assuming a constant experimental characteristic velocity $C^{\star}_{exp}$. However, the oxidizer-to-fuel ratio shift prevents to set this quantity. The authors have therefore noticed that $C^{\star}_{exp}$ error of 10 % leads to a discrepancy equal to 35 % for the instantaneous fuel regression rate. George *et al.*[32] developed a similar approach but considering a constant combustion efficiency during the firing test. In fact, in a set of repeatable realized tests,

the authors found very low variations of combustion efficiency around 1 % and below 2 % for all cases. The discrepancy between measured and computed space-averaged fuel port diameter at the end of a firing test varied below 2 %. By considering additional errors in pressure and temperature measurements and the computation of fuel mass flow rate, the uncertainty of fuel regression rate is below 3.5 %. Besides, George *et al.* have also assumed that the igniter combustion products do not contribute to the hybrid combustion process. In the present study, a catalytic injector is used to avoid the addition of fuel mass flow rate due to an igniter. Kumar and Ramakrishna[33] improved the methodology of George *et al.*[32] by considering convergence criteria such as the fuel mass flow rate for the oxidizer-to-fuel ratio for each time step and the final total mass for the combustion efficiency. Such an approach would improve computation stability and solution convergence. Nagata *et al.*[34] have also developed a ballistic reconstruction method based on constant combustion efficiency, applied to firing tests of CAMUI type hybrid rocket engines. The authors have noticed a decrease in errors when firing tests becomes longer. Those errors appear mainly from the unsteady mode during the ignition or the quenching. Using the same technique, Saito *et al.*[35] have compared the results of the ballistic reconstruction method with the data obtained from the measurement of the pressure drops through the solid-fuel in an axial-injection end-burning hybrid rocket. The ballistic reconstruction method shows a $\pm$ 10 % bias error of oxidizer-to-fuel ratio mainly due to the testing time and the uncertainties of the measurements of the oxidizer mass flow rate.

The instantaneous fuel regression rate evolution is obtained, in this study, by a ballistic reconstruction method based on the methodologies developed by Kumar and Ramakrishna[33] and Nagata *et al.*[34]. Consequently, during the firing test, combustion efficiency is assumed constant.

3.3.1. Ballistic reconstruction method: theoretical aspect

The ballistic reconstruction method is based on the formula describing the experimental characteristic velocity and combustion efficiency:

$$C^{\star}_{th}\left(O/F\right) = \frac{P_{ch} S_{throat}}{\eta_c \dot{m}_{tot}} \quad \text{and} \quad \eta_c = \frac{C^{\star}_{exp}}{C^{\star}_{th}} \tag{29}$$

The total fuel mass flow rate is expressed with the oxidizer-to-fuel ratio and the oxidizer mass flow rate:

$$\dot{m}_{tot} = \dot{m}_{ox}\left(1 + \frac{1}{O/F}\right) \tag{30}$$

An equation system with one unknown is therefore established (31). Knowing the instantaneous chamber pressure and oxidizer mass flow rate, the oxidizer-to-fuel ratio is obtained instantaneously. The g function can describe the total released energy in the combustion chamber per unit of injected oxidizer mass flow rate. This function depends on an efficiency part, related to the characteristic velocity, and an introduced fuel quantity part, related to $(1 + 1/(O/F))$. The theoretical characteristic velocity and the g function are therefore mainly dependent on the oxidizer-to-fuel ratio.

$$\begin{cases} \forall\ t \in [t_{ini}, t_{fin}]\ , \quad g\left(O/F\left(t\right)\right) = \dfrac{P_{ch}\left(t\right) S_{throat}}{\eta_c \dot{m}_{ox}\left(t\right)} \\ g : x \longmapsto g\left(x\right) = C^{\star}_{th}\left(x\right)\left(1 + \dfrac{1}{x}\right) \end{cases} \tag{31}$$

The theoretical characteristic velocity is obtained from the NASA chemical equilibrium program CEA[27] in specifying the temperature and species distribution for the oxidizer and the fuel, the chamber pressure, and the oxidizer-to-fuel ratio. The oxidizer temperature is hypothetically equal to the instantaneous temperature of the catalytic device within a range of 300 K. The fuel temperature is set at 950 K, assuming moderate variations. The chosen pressure is the instantaneous chamber pressure over a range of 4.4 MPa, starting from 0.6 MPa. The chosen fuel is the gaseous ethylene as pyrolysis product of the mixing between HDPE and the oxidizer is composed of steam water and gaseous oxygen, assuming a complete efficiency of the catalytic decomposition.

Besides, the g function is strictly decreasing (figure 14). In fact, in the considered configuration, the slope on the left side of the theoretical characteristic velocity optimum is slight enough to enable the $(1+1/(O/F))$ function to raise the g function without showing any local extremum.

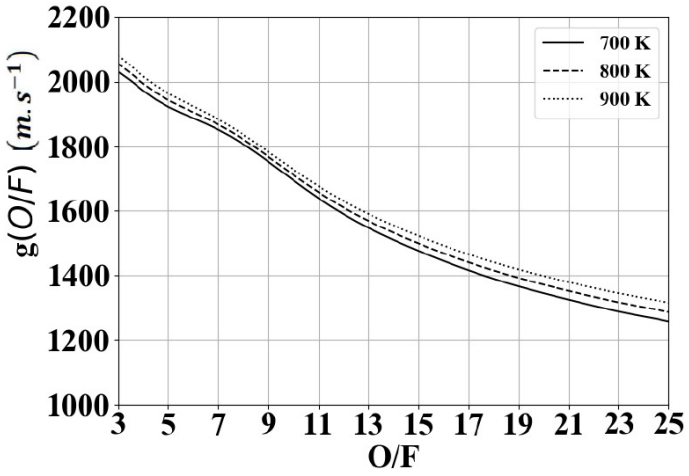

Figure 14: Sensitivity in temperature of the g function with the oxidizer-to-fuel ratio.

In other words, for an increase in oxidizer-to-fuel ratio from the stoichiometry, the characteristic velocity, and the decrease of fuel mass flow rate, considering a fixed oxidizer mass flow rate. Not only the fuel quantity decreases but also the efficiency decreases because of the oxidizer-to-fuel ratio distance from the stoichiometry. Decreasing the oxidizer-to-fuel ratio from the stoichiometry, the increase of fuel quantity reaches to compensate or even exceed the released energy losses per kilogram for a lower mixing quality. The g function strict monotony simplifies the resolution of the Newton method and warrants the solution uniqueness.

Hence, the total fuel mass flow rate can be instantaneously obtained from the value of the oxidizer-to-fuel ratio provided by the resolution of the equation system (31):

$$\dot{m}_{fuel} = \frac{\dot{m}_{ox}}{O/F} \tag{32}$$

3.3.2. Algorithm

The diagram 15 shows the algorithm solving the temporal evolution of the space-averaged fuel regression rate during the hybrid phase.

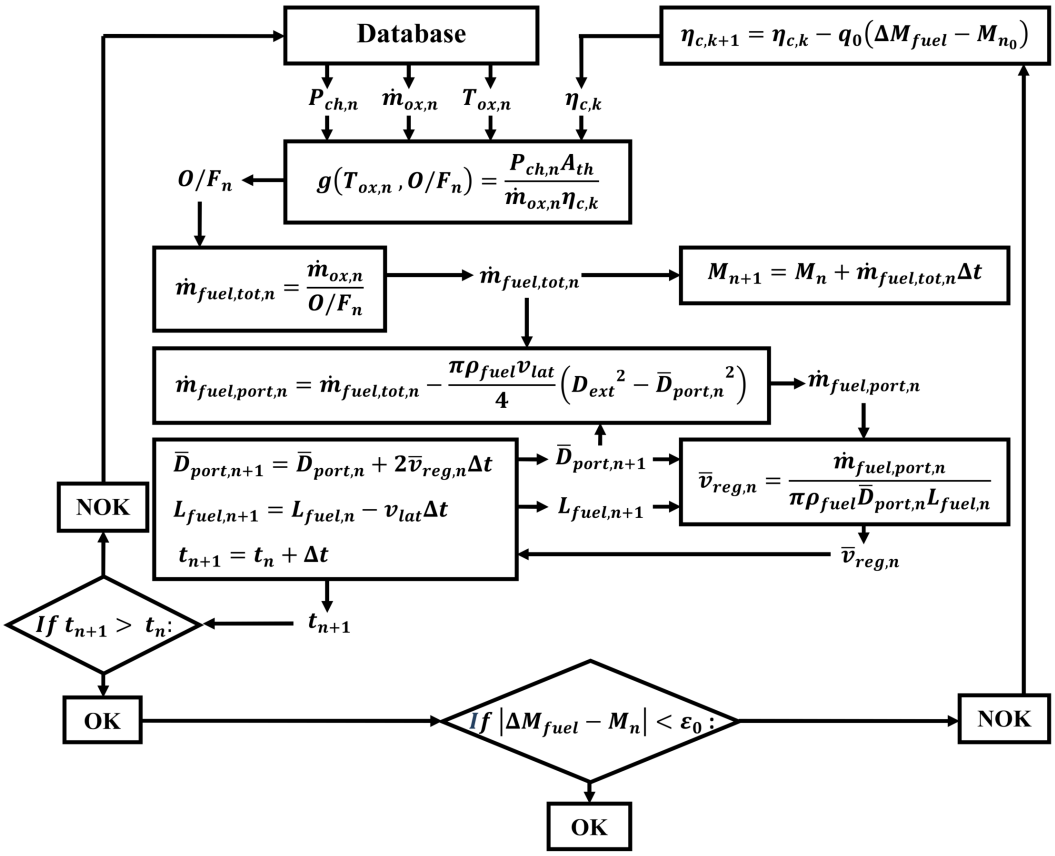

Figure 15: Methodology scheme of the used ballistic reconstruction method.

Because of the low values of fuel regression velocity observed for the HDPE (around 0.3-0.4 mm.s^{-1}), the regression on the head and rear ends of the solid-fuel cannot be neglected. Consequently, the fuel mass flow rate produced in the port is therefrom computed at the instant $t_n = n\Delta t$:

$$\dot{m}_{fuel,port,n} = \dot{m}_{fuel,n} - \rho_{fuel} v_{lat} \pi \frac{D_{ext}^2 - \overline{D}_{port,n}^2}{4} \tag{33}$$

At the instant t_n, the instantaneous space averaged fuel regression velocity in the port is computed, based on a port diameter $\overline{D}_{port,n}$, assumed invariant throughout the solid-fuel, and the fuel length $L_{fuel,n}$ (Figure 15). The solid-fuel geometry is then updated from the previous computed instantaneous quantities.

The parameter q_0 is a numerical constant used to enable the algorithm to converge. The value must be carefully chosen according to the processed firing test case. For a given combustion efficiency, the instantaneous fuel regression velocity calculation throughout the hybrid phase provides a total burnt mass amount. The combustion efficiency value is iteratively modified until the computed burnt mass converges to the experimental amount. Nevertheless, the convergence can be reached with one or two iterations by using a combustion efficiency estimation from experimental data. The convergence criteria are based on the uncertainty of the measurement of the total burnt mass.

3.3.3. Application

The ballistic reconstruction method is therefore applied to HYCAT firing tests considered in the present study. The chamber pressure is obtained from the measurements of pressure sensors located upstream of the solid-fuel. The instantaneous space-averaged fuel regression rate and fuel port diameter are shown in Figure 16. A quasi-linear increase of the fuel port diameter is observed.

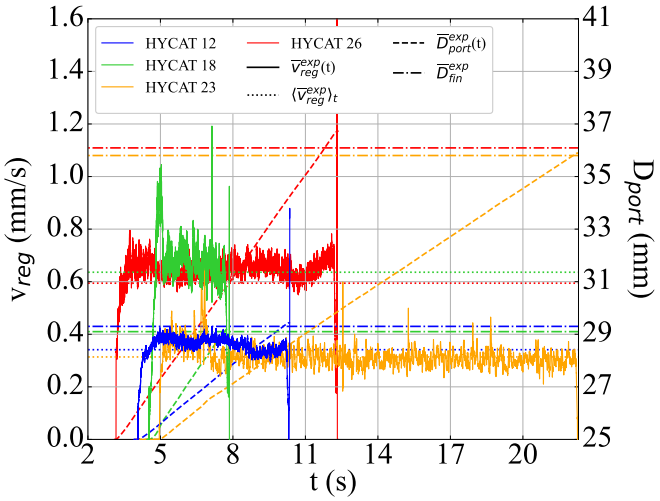

Figure 16: Instantaneous fuel regression rate and port diameter evolutions during the firing test for the selected HYCAT cases.

For the 12^{th} HYCAT firing test, the instantaneous spatially averaged fuel regression velocity shows a stable evolution during the hybrid phase. Nevertheless, despite noised variations, the global trend slightly oscillates with a period roughly equal to half of the burning time. For the three other cases, the fuel regression velocity evolution level decreases steeply after 1 or 2 s from the beginning of the hybrid phase. For the HYCAT 18 and 26 firing tests, the fuel regression level is twice higher than the one found in HYCAT 12 and 23 cases, with a mean value. For the HYCAT 18 firing test, the flow inertia effects improve the mixing, thicken the flame, and increase the temperature gradient at the fuel surface[36, 37]. For the HYCAT 26 firing test, with an oxidizer mass flow rate twice higher than for the HYCAT 12 and 23 firing tests, the convection is also enhanced due to a much higher total mass flow rate through the port, according to the diffusion-limited theory of Marxman and Gilbert[1].

For the HYCAT 26 firing test case, the ballistic reconstruction model is improved to take into account the throat section surface evolution from a chosen

instant corresponding to the start of the erosion phenomenon t_{erod}. The chosen erosion onset time corresponds to the instant associated with the beginning of the chamber pressure decrease before the end of the firing test due to the throat erosion effects (Figure 4). The evolution of the throat section surface is approached linearly during the erosion phase:

$$\begin{cases} \forall t \in [t_{erod}, t_{fin}] \ , \quad g\left(O/F\left(t\right)\right) = \dfrac{P_{ch}\left(t\right) S_{throat}\left(t\right)}{\eta_c \dot{m}_{ox}\left(t\right)} \\ S_{throat}\left(t\right) = \left(S_{throat}^{fin} - S_{throat}^{ini}\right) \dfrac{t - t_{erod}}{t_{fin} - t_{erod}} + S_{throat}^{ini} \end{cases} \tag{34}$$

During the hybrid phase, the fuel regression rate trend is globally stable despite a slight drop at t = 10.9 s.

3.3.4. Error analysis

A sensitivity analysis is carried out on the ballistic reconstruction method, based on the HYCAT 12 firing test case. The study aims at assessing the main source of errors and biases of the method used to obtain the fuel mass flow rate time-evolution. Table 5 shows the sensitivity of the main parameters of the ballistic reconstruction method.

Table 5: Sensitivity analysis for the ballistic reconstruction method.

Case	X_{ref}	δX	$\epsilon\left(\overline{v}_{reg}\right)$ (%)	$\epsilon\left(\overline{D}_{port}\right)$ (%)
t_{hyb}	6.3 s	+0.4 s	$<$ 9.6 (from t = 4.2 s)	$<$ 1.3
T_{ox}	$T_{ox}\left(t\right)$	600-$T_{ox}\left(t\right)$ K	$\approx$ 1.7 (t = 4.5 to 10 s), $>$ 4 otherwise	$<$ 0.1
T_{fuel}	900 K	+100 K	$<$ 0.1	$<$ 0.01

The uncertainty of the instantaneous fuel regression rate is higher than the one related to the burning time. Thus, the assessment of the burning time is decisive for the accuracy of the instantaneous spatially averaged fuel regression rate obtained by the ballistic reconstruction method.

The difference in the oxidizer temperature shows a fair discrepancy in fuel regression rate. Hence, the impact of the oxidizer temperature cannot be neglected. As measurement on the fuel surface is not feasible with the considered set-up,

the impact of the fuel surface temperature requires assessment. The differences in fuel regression rate turn out very small showing the neglectable impact of the fuel surface temperature. Such an insensitivity would result from a high oxidizer-to-fuel ratio of the presented firing test ($O/F = 12.4$).

About chamber pressure, with a difference of 0.4 MPa, the g function displays very little alteration. Nevertheless, a discrepancy of 0.8 % is observed over a range of oxidizer-to-fuel ratio between 6 and 11.

The final port diameter provided by the ballistic reconstruction method manages to represent the space averaged final port diameter obtained by direct measurement in the solid-fuel port conduct (table 6).

Table 6: Comparison between the measured and the rebuilt port diameter for the selected HYCAT firing tests.

Case	HYCAT 12	HYCAT 18	HYCAT 23	HYCAT 26
$\overline{D}_{fin}^{exp}$ (mm)	29.1 ± 0.3	29.1 ± 0.1	35.8 ± 0.4	36.1 ± 0.7
$\overline{D}_{fin}$ rebuilt (mm)	29.4	29.3	35.9	36.7
ϵ (%)	1.0	0.7	0.3	1.7

The rebuilt results show that, using the direct measurement technique, the rebuilt port diameter discrepancy is below the uncertainty except for the HYCAT 18 firing test. Nevertheless, the value remains in good agreement with the experiment. The rebuilt diameter value can henceforth be used to estimate the experimental fuel regression velocity averaged spatially and temporally.

The discrepancies come mainly from the hybrid phase time. Even though ΔM_{fuel} takes into account all mass losses during the ring test, the actual mass loss during the hybrid phase is necessarily lower due to the burnt fuel mass during the mono-propellant phase and just after the oxidizer valve closing. The final fuel port diameter, computed by the ballistic reconstruction algorithm, could be overestimated. Besides, due to these fuel surface heterogeneities, the

experimental final length of the solid-fuel is also difficult to obtain accurately. Errors may be inserted due to an approximate value of face fuel regression rates, assumed constant throughout the firing test.

For the HYCAT 26 firing test, the uncertainty of the final port diameter averaged spatially is the highest amongst all the considered cases. In fact, the measurement uncertainties of the local final port diameter, beyond z = 150 mm, are anomalously higher than for the other measurement positions. The main reason comes from the wave pattern carved on the fuel port surface which disturbs the micrometer positioning for measurements.

4. Validation, application, & discussion

4.1. Validation of the methodology: comparison with ultrasonic sensor data

The proposed methodology is assessed by comparing the results with the fuel regression velocity time-evolution obtained by the ultrasonic measurement technique. The validation process is illustrated by the HYCAT 12 case at the ultrasonic sensor position the closest to the solid-fuel top face: z = 75 mm from the solid-fuel head face at the initial state (figure 17). The sampling frequency f_s is 60 MHz. The pulse repetition period Δt_{mes} is equal to 5×10^{-4} s. The HDPE is The fuel regression rate calculation is determined classically by the expression:

$$v_{reg}^{US}(t) = -\frac{C_0}{2}\frac{d\tau_{tof}}{dt}(t) \tag{35}$$

The sound speed C_0 is obtained by considering the time-of-flight t_{tof} (s) and the solid-fuel thickness at the initial state.

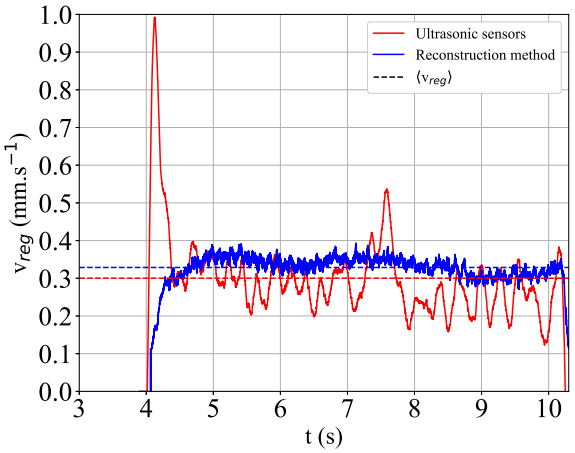

Figure 17: HYCAT 12 case: fuel regression rate comparison between ultrasonic sensor and reconstruction technique results.

The mean value of the temporal fuel regression rate, obtained with the ultrasonic measurement technique, is 8.6 % lower than obtained with the restitution technique. The ballistic reconstruction method uses the final mass loss possibly overestimated due to the burnt time assessment. The fuel regression rate level may overestimate the actual value to reach the targeted mass loss quantity.

The ultrasonic sensors get the fuel regression rate directly at z = 75 mm, where the value is very high during a short time just after the ignition. This behavior indicates that the fuel port conduct may enlarge sooner than given by the ballistic reconstruction method, not showing any peak of fuel regression rate during the ignition. Nevertheless, except at the beginning of the hybrid phase, both methods display the same global trends: a fuel regression rate peak, observed around t = 7.5 s.

The ultrasonic data shows higher fuel regression rate oscillations and lower related frequencies compared with the restitution method. The instantaneous fuel mass flow rate, used in the restitution method, gives a global time evolu-

tion of solid-fuel consumption. In contrast, the ultrasonic sensor provides direct instantaneous data. Hence, with the given data is not possible to determine the actual local time evolution accurately, even though the global trends and the time-averaged level of fuel regression rate are reasonably in good agreement with the ultrasonic data.

Nevertheless, the present methodology aims at improving the instantaneous fuel port diameter profile throughout the solid-fuel to provide instantaneous geometry configuration for CFD computations.

4.2. Application of the methodology

The restitution method is applied for the firing test cases HYCAT 12, 18, 23 and 26. For each firing test, Λ_0 is computed and three instants are chosen to be able to see the time and space variations of the port diameter and the fuel regression rate.

For the HYCAT 12 firing test, the profiles of port diameter and fuel regression velocity throughout the port are shown for the chosen instants t = 5.5 s, t = 7.5 s and t = 9.5 s in the figure 18. The fuel mass flow rate fraction is computed between z = 12 mm and z = 235 mm, and equal to $\Lambda_0 = 0.87$. The minimal bound is chosen to avoid the bulge region around z = 9 mm (Figure 12) because the assessment of the fuel mass flow rate, used as input, is hypothetically due to the solid-fuel degradation in the port conduct only. Thereby, the quantity of melted HDPE brought by the flow from the solid-fuel top face is not taken into account in the restitution method. As expected, the port diameter profile evolves from the initial cylindrical form to the final surface form, fitting to measurements taken on the solid-fuel port surface. For the fuel regression velocity profiles, the magnitude follows the same trend as the instantaneous spatial averaged fuel regression velocity observed in the figure 16. Besides, throughout the port, a significant decrease is observed close to the port outlet, leading to smaller port diameters.

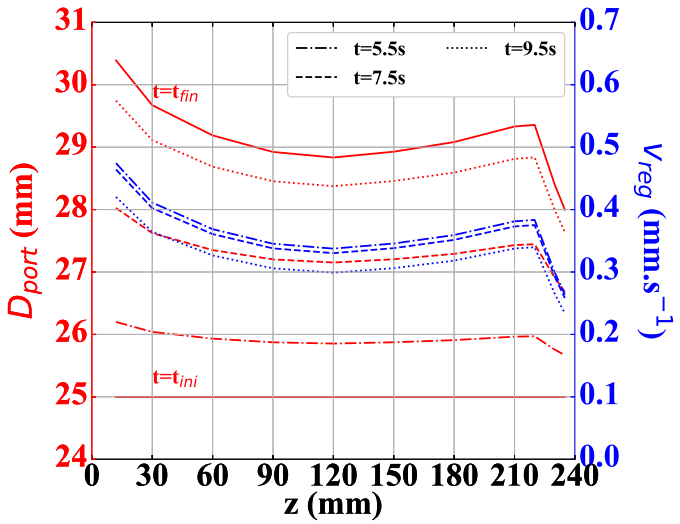

Figure 18: HYCAT 12: Instantaneous evolutions of port diameter and fuel regression profiles throughout the fuel port during the hybrid phase.

For the HYCAT 18 firing test, the profiles of port diameter and fuel regression velocity throughout the port are shown for the chosen instants t = 5 s, t = 6 s, and t = 7 s in Figure 19. The fuel mass flow rate fraction is computed between z = 3 mm and z = 239 mm, and equal to $\Lambda_0 = 0.90$. This fraction value is higher than the one related to the HYCAT 12 case because the considered port part is more extended at the end borders. At t = 5 s, the port diameter profile remains very close to the initial state. However, the fuel regression rate level is the highest amongst all the hybrid phase according to the rebuilt evolution of the instantaneous fuel regression rate (figure 16). Hence, the wall heat flux at the inlet region is very high and can be related to the particular boundary layer in a swirling flow. The flow inertia enables to improve the species mixing and to thicken the flame. Hence, the energy transported by turbulent viscosity is very soon optimal, which leads to high wall heat flux from the beginning of the port.

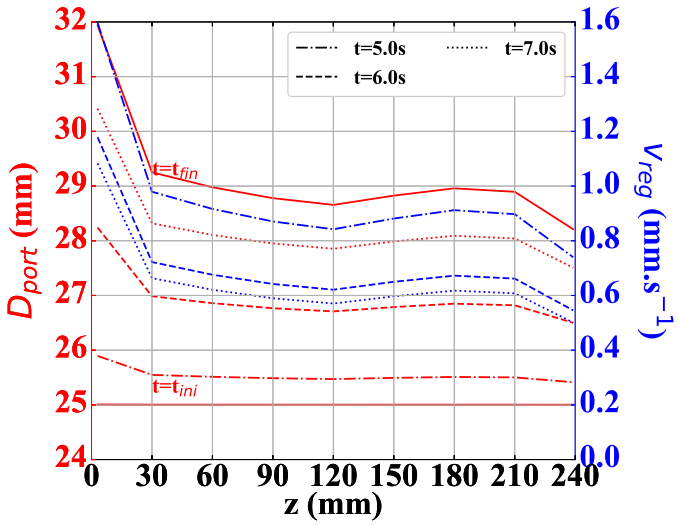

Figure 19: HYCAT 18: Instantaneous evolutions of port diameter and fuel regression profiles throughout the fuel port during the hybrid phase.

The fuel regression rate level is almost twice higher than for the axial configuration. At t = 6 s, the fuel regression rate lessens. At t = 7 s, the port diameter keeps the same shape even though the global value increases. The fuel regression rate profile remains very stable in form and magnitude.

For the HYCAT 23 firing test, the profiles of port diameter and fuel regression velocity throughout the port are shown for the chosen instants t =10 s, t = 14 s and t = 18 s in the figure 20. The fuel mass flow rate fraction is computed between z = 13 mm and z = 233 mm, and equal to $\Lambda_0 = 0.90$.

Surprisingly, the fraction of the fuel mass flow rate is higher than for the HYCAT 12 firing test even though the considered port conduct part is shorter according to the engine axis. This difference might be due to the small mass losses because of the low fuel regression level in the bulge regions at the inlet and the outlet. Besides, another reason would be the long burning time.

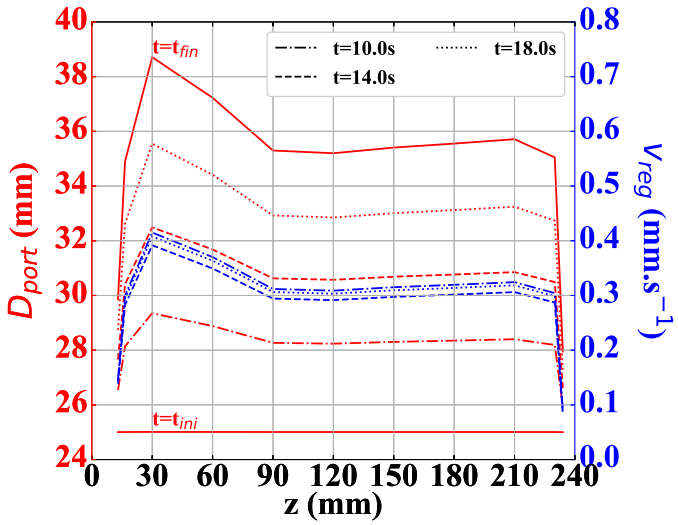

Figure 20: HYCAT 23: Instantaneous evolutions of port diameter and fuel regression profiles throughout the fuel port during the hybrid phase.

The port diameter profiles show a regular increase because of a stable level of fuel regression rate during the firing test. The growth of the cavity close to the inlet is due to a higher value of fuel regression rate. The port part between the half to the outlet does not display the expected trend in fuel regression rate. This observation means that the fuel mass addition effect in the fuel regression velocity behavior is insignificant and, therefore, not coherent with the explanation of the fuel regression distribution given by Chiaverini[28]. Nevertheless, because the burning time of the HYCAT 23 case much larger than the one of the HYCAT 12 case, the final diameter is larger as well. According to Houser and Peck[38], the rise with the axial distance of the fuel regression rate is more attenuated when the fuel port diameter increases. Beyond a critical value, this fuel regression increase is no longer held. The final port diameter is therefore too altered to validate the assumption about the proportionality between the instantaneous and final port diameter variations during the firing test. Thus, the burning time is a limiting parameter for the restitution method.

For the HYCAT 26 firing test, the profiles of port diameter and fuel regression velocity throughout the port are shown for the chosen instants t = 4 s, t = 7.5 s, and t = 11 s in the figure 21. The fuel mass flow rate fraction is computed between z = 1 mm and z = 238 mm, and equal to $\Lambda_0 = 0.91$. Because of an oxidizer mass flow rate twice higher compared to the other cases, the fuel regression rate is also much higher according to diffusion-limited theory.

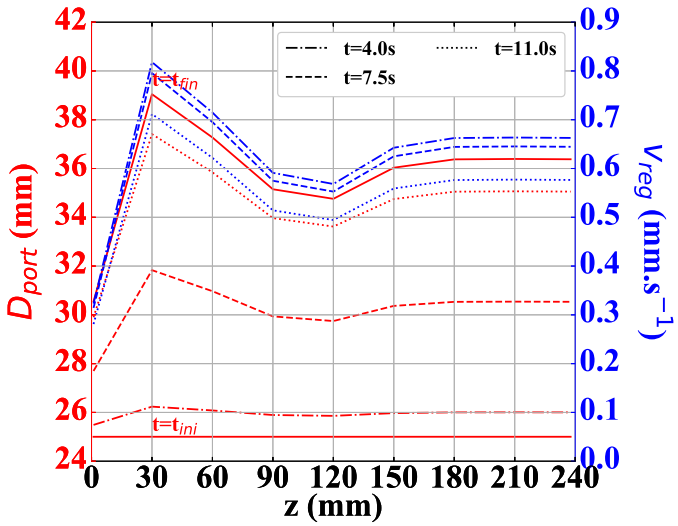

Figure 21: HYCAT 26: Instantaneous evolutions of port diameter and fuel regression profiles throughout the fuel port during the hybrid phase.

The level of fuel regression rate remains stable during the firing test. However, the results must be taken very carefully because of the particular degradation mode between z = 150 mm to the outlet, characterized by a wave-patterned surface. Hence, the port diameter evolution is not warranted.

Furthermore, the uncertainty of the results obtained by the restitution method is not assessed and very difficult to establish due to the strong assumptions related to the energy equation. Hence, all these results can be viewed qualitatively only, considering the limitation imposed by the assumptions. Nevertheless, such a method can be considered as a first approach to design a numerical firing test

configuration, related to an instant, for CFD simulation.

5. Conclusion

A post-processing tool is developed to rebuild the behavior of the fuel regression rate instantaneously and locally throughout the fuel port during the firing test. The hybrid rocket HYCAT testing campaign, using a catalytic injector, is considered to establish a representative sample treated by the post-processing tool. The restitution method used the final fuel port diameter measurement throughout the solid fuel and the instantaneous fuel mass flow rate in the port conduct. This data is obtained by the ballistic reconstruction technique, improved to take into the particularities of the hybrid rocket engine HYCAT. For all cases, the profiles of the instantaneous port diameter are rebuilt and show the ability of the methodology to restitute the space and time distribution of the fuel port diameter.

However, the fuel regression rate distributions show some limitations of the method even though the average is coherent with the ballistic reconstruction trends. Some strong assumptions prevent the assessment of the uncertainties related to the restitution method. The spatial and temporal fuel regression rate distribution could thereby offer only a qualitative view. Nevertheless, the presented methodology is sufficient to improve CFD simulation results by providing a more realistic fuel port diameter profile at a particular instant of the firing test.

The proportionality link between instantaneous and final port diameter variations assumes that the variations of spatial variations of the flame and wall heat flux are kept during the firing test and printed on the fuel surface. However, such an assumption needs an experimental assessment. Most probably, the energy equation of instantaneous fuel port diameter variations requires improvements to take into account the subtler effects of flame and the flow.

The mathematical container needs improvement. The homotopy properties between the initial and the final fuel surfaces would be interesting to study. A

better mathematical formulation would lead to a simpler approach to fuel regression rate distribution spatially and temporally. With an experimental study, the relative behavior of the flame and the wall heat flux can provide useful equations to improve the system. Besides, a 1D or 2D model coupled with the restitution method could improve the representativeness of the port diameter axial variations.

The fraction of fuel mass flow rate in a port part is assumed constant during the firing test. This strong assumption is due to a lack of information about the time evolution of the fuel mass flow rate in the port part. An approach to be tested is to used the ultrasonic sensors to take locally a fuel regression rate value which can be used, by the analytical expressions provided by the restitution method, to obtain an instantaneous value of the fraction of fuel mass flow rate in the port part.

Nevertheless, the restitution method developed here is the first approach for a more elaborated post-processing tool to measure the time and space distributions of the fuel regression rate and port surface during the firing test.

Declaration of Competing Interest

None declared.

Acknowledgments

This research is supported by ONERA and Région Occitanie, award no. DESR-SRI/15066464.

References

[1] G. Marxman, M. Gilbert, Turbulent boundary layer combustion in the hybrid rocket, Symposium (International) on Combustion 9 (1) (1963) 371–383. doi:10.1016/s0082-0784(63)80046-6.

[2] N. Bellomo, M. Lazzarin, F. Barato, M. Grosse, Numerical investigation of the effect of a diaphragm on the performance of a hybrid rocket motor, in: 46th AIAA/ASME/SAE/ASEE Joint Propulsion Conference & Exhibit, American Institute of Aeronautics and Astronautics, 2010. doi:10.2514/6.2010-7033.

[3] H. Tian, X. Li, N. Yu, G. Cai, Numerical and experimental investigation on the effects of aft mixing chamber diaphragm in hybrid rocket motor, Science China Technological Sciences 56 (11) (2013) 2721. doi:10.1007/s11431-013-5325-z.

[4] D. Bianchi, F. Nasuti, D. Delfini, Modeling of gas-surface interface for paraffin-based hybrid rocket fuels in cfd, in: 6th European Conference for Aerospace Science, Rhode-Saint-Genèse, 2015. doi:FP_EUCASS-368.

[5] D. Bianchi, P. Lapenna, F. Creta, F. Nasuti, Numerical simulations of flowfield and combustion in hybrid rockets, in: Space Propulsion Conference, 2016. doi:SP2016-3125219.

[6] D. Bianchi, G. Leccese, F. Nasuti, C. C., Modeling of high density polyethylene regression rate in the simulation of hybrid rocket flowfields, in: 7th European Conference for Aeronautics and Space Sciences, no. 629, Rhode-Saint-Genèse, 2017. doi:10.13009/EUCASS2017-629.

[7] G. Cai, P. Zeng, X. Li, H. Tian, N. Yu, Scale effect of fuel regression rate in hybrid rocket motor, Aerospace Science and Technology 24 (1) (2013) 141–146. doi:10.1016/j.ast.2011.11.001.

[8] A. Coronetti, W. Sirignano, Numerical analysis of hybrid rocket combustion, Journal of Propulsion and Power 29 (2) (2013) 371–384. doi:10.2514/1.B34760.

[9] E. Farbar, J. Louwers, T. Kaya, Investigation of metallized and non-metallized hydroxyl terminated polybutadiene/hydrogen peroxide hybrid

rockets, Journal of Propulsion and Power 23 (2) (2007) 476–486. doi:10.2514/1.22091.

[10] G. Gariani, F. Maggi, L. Galfetti, Numerical simulation of htpb combustion in a 2d hybrid slab combustor, Acta Astronautica 69 (5–6) (2011) 289–296. doi:10.1016/j.actaastro.2011.03.015.

[11] G. Leccese, D. Bianchi, F. Nasuti, Simulations of hybrid rocket flowfields including modeling of fuel pyrolysis and thermal radiation, in: Space Propulsion Conference, 2016.

[12] F. Shan, L. Hou, Y. Piao, Combustion performance and scale effect from n2o/htpb hybrid rocket motor simulations, Acta Astronautica 85 (2013) 1–11. doi:10.1016/j.actaastro.2012.12.013.

[13] H. Tian, Y. Li, C. Li, X. Sun, Regression rate characteristics of hybrid rocket motor with helical grain, Aerospace Science and Technology 68 (2017) 90 – 103. doi:10.1016/j.ast.2017.05.006.

[14] S. Zhang, F. Hu, D. Wang, P. Okolo.N, W. Zhang, Numerical simulations on unsteady operation processes of N2O/HTPB hybrid rocket motor with/without diaphragm, Acta Astronautica 136 (2017) 115 – 124. doi:https://doi.org/10.1016/j.actaastro.2017.03.005.

[15] G. Di Martino, S. Mungiguerra, C. Carmicino, R. Savino, Combined fluid-dynamic modelling of hybrid rocket internal ballistics and nozzle heat transfer, in: 7th European Conference for Aeronautics and Space Sciences, Rhode-Saint-Genèse, 2017. doi:10.13009/EUCASS2017-611.

[16] G. Di Martino, S. Mungiguerra, C. Carmicino, R. Savino, Computational fluid-dynamic modeling of the internal ballistics of paraffin-fueled hybrid rocket, Aerospace Science and Technology 89 (2019) 431 – 444. doi:10.1016/j.ast.2019.04.019.

[17] C. Kumar, A. Kumar, Effect of diaphragms on regression rate in hybrid rocket motors, Journal of Propulsion and Power 29 (3) (2013) 559–572. doi:10.2514/1.b34671.

[18] C. Carmicino, S. A. Russo, Influence of a conical axial injector on hybrid rocket performance, Journal of Propulsion and Power 22 (5) (2006) 984–995. doi:10.2514/1.19528.

[19] J.-Y. Lestrade, J. Messineo, J. Anthoine, A. Musker, F. Barato, Development and test of an innovative hybrid rocket combustion chamber, in: 7th European Conference for Aeronautics and Space Sciences, no. 414, Rhode-Saint-Genèse, 2017. doi:10.13009/EUCASS2017-414.

[20] J. Anthoine, J.-Y. Lestrade, S. Messineo, J.and Casu, Performances of a multi-pulsed hybrid rocket engine operating with highly concentrated hydrogen peroxide, in: 53rd AIAA/SAE/ASEE Joint Propulsion Conference, Paper AIAA 2017–4906, Atlanta, GA, 2017. doi:10.2514/6.2017-4906.

[21] C. Carmicino, A. Sorge, Performance comparison between two different injector configurations in a hybrid rocket, Aerospace Science and Technology 11 (1) (2007) 61 – 67. doi:10.1016/j.ast.2006.08.009.

[22] A. Russo Sorge, A. Esposito, G. Quaranta, G. Torella, Regression rate measurements in a hybrid rocket, in: 36th AIAA/ASME/SAE/ASEE Joint Propulsion Conference & Exhibit, AIAA Paper 2000–3438, Las Vegas, NV, 2000. doi:10.2514/6.2000-3438.

[23] J.-Y. Lestrade, J. Anthoine, O. Verberne, A. J. Boiron, G. Khimeche, C. Figus, Experimental demonstration of the vacuum specific impulse of a hybrid rocket engine, Journal of Spacecraft and Rockets 54 (1) (2017) 101–108. doi:10.2514/1.a33467.

[24] J.-Y. Lestrade, P. Prévot, J. Messineo, J. Anthoine, S. Casu, B. Geiger, Development of a catalyst for high concentrated hydrogen peroxide, in: 6th

International Symposium on Propulsion for Space Transportation (Space Propulsion), SP2016–3125136, 2016.

[25] C. Carmicino, A. Russo Sorge, Role of injection in hybrid rockets regression rate behavior, Journal of Propulsion and Power 21 (4) (2005) 606–612. doi:10.2514/1.9945.

[26] A. Savitzky, M. J. E. Golay, Smoothing and differentiation of data by simplified least squares procedures, Analytical Chemistry 36 (8) (1964) 1627–1639. doi:10.1021/ac60214a047.

[27] S. Gordon, B. J. McBride, Computer program for calculation of complex chemical equilibrium compositions and applications, Tech. rep., NASA, nASA-RP-1311 (1994).

[28] M. Chiaverini, Review of solid-fuel regression rate behavior in classical and nonclasical hybrid rocket motors, in: Fundamentals of Hybrid Rocket Combustion and Propulsion, Vol. 218, Progress in Astronautics and Aeronautics, edited by Chiaverini, M. and Kuo, K., 2007, Ch. 2, pp. 37–126. doi:10.2514/5.9781600866876.0037.0126.

[29] H. Koo, K. O. Mon, C. Lee, Effect of a block on flow oscillations near evaporating solid fuel surface, Aerospace Science and Technology 30 (1) (2013) 269 – 277. doi:https://doi.org/10.1016/j.ast.2013.08.011. URL http://www.sciencedirect.com/science/article/pii/S127096381300151X

[30] A. Russo Sorge, C. Carmicino, Non-intrusive regression rate measurements in a hybrid rocket, RTO AVT (33) (2002) 1–14, rTO-MP-091.

[31] E. J. Wernimont, S. D. Heister, Reconstruction technique for reducing hybrid-rocket combustion test data, Journal of Propulsion and Power 15 (1) (1999) 128–136. doi:10.2514/2.5401.

[32] P. George, S. Krishnan, P. M. Varkey, M. Ravindran, L. Ramachandran, Fuel regression rate in hydroxyl-terminated-polybutadiene/gaseous-oxygen

hybrid rocket motors, Journal of Propulsion and Power 17 (1) (2001) 35–42. arXiv:https://doi.org/10.2514/2.5704, doi:10.2514/2.5704.

[33] R. Kumar, P. Ramakrishna, Measurement of regression rate in hybrid rocket using combustion chamber pressure, Acta Astronautica 103 (2014) 226 – 234. doi:10.1016/j.actaastro.2014.06.044.

[34] H. Nagata, H. Nakayama, M. Watanabe, M. Wakita, T. Totani, Accuracy and applicable range of a reconstruction technique for hybrid rockets, Advances in aircraft and spacecraft science 1 (3) (2014) 273–289. doi:10.12989/AAS.2014.1.3.273.

[35] Y. Saito, L. T. Kamps, K. Komizu, D. Bianchi, F. Nasuti, H. Nagata, The accuracy of reconstruction techniques for determining hybrid rocket fuel regression rate, in: 2018 Joint Propulsion Conference, AIAA 2018–4923, 2018. doi:10.2514/6.2018-4923.

[36] N. Bellomo, M. Faenza, F. Barato, A. Bettella, D. Pavarin, The "vortex reloaded" project: Numerical investigation on fully tangential vortex injection in n2o - paraffin hybrid motors, in: 48th AIAA/ASME/SAE/ASEE Joint Propulsion Conference & Exhibit 2012, 2012. doi:10.2514/6.2012-3903.

[37] E. Paccagnella, F. Barato, D. Pavarin, A. Karabeyoğlu, Scaling parameters of swirling oxidizer injection in hybrid rocket motors, Journal of Propulsion and Power (2017) 1–17doi:10.2514/1.b36241.

[38] T. Houser, M. Peck, Research in hybrid combustion, in: H. G. Wolfhard, I. Glassman, L. Green (Eds.), Heterogeneous Combustion, Vol. 15 of Progress in Astronautics and Rocketry, Elsevier, 1964, pp. 559 – 581. doi:https://doi.org/10.1016/B978-1-4832-2730-6.50027-0.